

Article

Ultra-Thin and Lithography-Free Transmissive Color Filter Based on Doped Indium Gallium Zinc Oxide with High Performance

Xiangrui Fan ¹, Shengyao Wang ², Dongdong Xu ² and Gaige Zheng ^{2,3,*}

¹ School of Electronics & Information Engineering, Nanjing University of Information Science & Technology, Nanjing 210044, China; jsmetamaterials@163.com

² Jiangsu Collaborative Innovation Center on Atmospheric Environment and Equipment Technology (CICAEET), Nanjing University of Information Science & Technology, Nanjing 210044, China; syaowang2022@163.com (S.W.); ddongxu2022@163.com (D.X.)

³ Jiangsu Key Laboratory for Optoelectronic Detection of Atmosphere and Ocean, School of Physics and Optoelectronic Engineering, Nanjing University of Information Science & Technology, Nanjing 210044, China

* Correspondence: jsnanophotonics@yahoo.com

Abstract: A kind of ultra-thin transmissive color filter based on a metal-semiconductor-metal (MSM) structure is proposed. The displayed color can cover the entire visible range and switches after H₂ treatment. An indium gallium zinc oxide (IGZO) semiconductor was employed, as the concentration of charge carriers can be controlled to adjust the refractive index and achieve certain colors. The color modulation in the designed structure was verified using the rigorous coupled wave analysis (RCWA) method. The angular independence of the relative transmission could reach up to 60°, and polarization-insensitive performance could also be maintained. Numerical results demonstrated that the thickness of IGZO was the key parameter to concentrate the incident light. The overall structure is planar and lithography-free and can be produced with simple preparation steps. The obtained results can also be extended to other similar resonators where a proper cavity allows dynamical functionality.

Keywords: color filter; indium gallium zinc oxide; lithography-free

Citation: Fan, X.; Wang, S.; Xu, D.; Zheng, G. Ultra-Thin and Lithography-Free Transmissive Color Filter Based on Doped Indium Gallium Zinc Oxide with High Performance. *Micromachines* **2022**, *13*, 1228. <https://doi.org/10.3390/mi13081228>

Academic Editor(s): Giampaolo Mistura and Aiqun Liu

Received: 14 June 2022

Accepted: 28 July 2022

Published: 31 July 2022

Publisher's Note: MDPI stays neutral with regard to jurisdictional claims in published maps and institutional affiliations.



Copyright: © 2022 by the authors. Licensee MDPI, Basel, Switzerland. This article is an open access article distributed under the terms and conditions of the Creative Commons Attribution (CC BY) license (<https://creativecommons.org/licenses/by/4.0/>).

1. Introduction

As an important part of optoelectronic devices, color filters are widely used in color printing [1–3], high-resolution displays [4,5], sustainable color decoration [6,7] and safety colors [8]. Potential applications have aroused great interest in recent years. It is well-known that the color characteristics of traditional dye filters and pigment filters are determined by the inherent absorbance of their constituent materials [9,10]. In this context, the performance can be easily affected by high-intensity permanent light illumination and various chemical processes. As a result, the performance can be greatly reduced [11]. Color filters made from functional nanostructures rely on the interactions between light and the device, with the advantages of high efficiency, high spatial resolution and good stability [12].

Research on color filters has mainly been concentrated on areas such as surface plasmon resonance (SPR) [13,14], guided mode resonance (GMR) [15,16] and Mie resonance [17–19]. Transmitted or reflected color filters with dynamic management have been realized by changing the shape and structural parameters [20,21]. Although these nanostructure-based filters can achieve high performance, the color usually cannot be switched. The performance of nanostructures and thin films can be adjusted using the polarization state of incidence [22–25]. Phase change materials (PCMs) have also been widely used to

achieve color switching. $\text{Ge}_2\text{Sb}_2\text{Te}_5$ [26] and VO_2 [27] are common PCMs, and their permittivity can be changed by controlling the temperature to produce a phase change. However, this effect occurs in the near-infrared band and cannot be freely applied to the visible light range. Furthermore, WO_3 [28] and indium tin oxide (ITO) [29] can also undergo phase changes with changes in the applied voltage. The refractive index can also be influenced by the carrier concentration, which is much faster and more efficient [30].

In this paper, a new Fabry–Perot (F-P)-type transmissive color filter is proposed that can achieve structural colors with high efficiency using IGZO embedded between the metal Ag mirrors. By changing the thickness of the IGZO, high-purity structural colors can be obtained, and the carrier concentration can be changed using H_2 treatment to control the refractive index of the IGZO, thereby achieving color switching in the visible range. The proposed color filter also presents incident angle-insensitive and polarization-independent performances. There are two advantages of this filter: high purity and faster switching speed.

2. Model and Methods

IGZO is a semiconductor that is widely used in neuromorphic electronic devices and flexible displays [31–33]. It has excellent electro-optical properties and many advantages with great potential for application in photonic devices. The electron density can be controlled by the H_2 plasma treatment process, which generates free electrons as the injected hydrogen atoms form O-H bonds with the ionized oxygen in IGZO, as follows [34]:



The dielectric constant of IGZO is expressed by the Tauc–Lorentz–Drude model [35,36]:

$$\epsilon_{\text{IGZO}} = \epsilon_{\text{TL}} + \epsilon_{\text{D}} = \epsilon_1 + i\epsilon_2 \quad (2)$$

Here, ϵ_{TL} and ϵ_{D} represent the dielectric constants given by the Tauc–Lorentz and Drude models, respectively, and the Drude term describes the free electron absorption.

The complex permittivity of the Drude model is expressed as [34,36]:

$$\epsilon_{\text{D}}(E) = -\frac{A_{\text{D}}}{E^2 + \Gamma_{\text{D}}^2} - \left(\frac{A_{\text{D}}\Gamma_{\text{D}}}{E^3 + \Gamma_{\text{D}}^2 E}\right)i \quad (3)$$

Here, A_{D} is the amplitude and Γ_{D} is the broadening parameter, respectively expressed as:

$$A_{\text{D}} = \epsilon_{\infty} E_{\text{p}}^2 = \epsilon_{\infty} \hbar^2 \omega_{\text{p}}^2 \quad (4)$$

$$\Gamma_{\text{D}} = \hbar\gamma, \gamma = \frac{e}{m^* \mu} \quad (5)$$

Here, γ represents the angular frequency, μ is the broadening parameter of light mobility, E_{p} is the plasma energy, ϵ_{∞} is the high-frequency dielectric constant, \hbar is the Planck constant and e is the electronic charge. ω_{p} is the plasma angular frequency, expressed as:

$$\omega_{\text{p}} = \left(\frac{e^2 N}{m^* \epsilon_{\infty} \epsilon_0}\right)^{1/2} \quad (6)$$

where N is the photocarrier concentration and ϵ_0 is the free space permittivity.

The refractive index of IGZO can be changed through H_2 plasma treatment. After treatment, the refractive index of IGZO decreases by ~ 0.4 , and the extinction coefficient also changes. This is due to the change in the electron density in the film. The electron

density of the low-conductivity film is less than 10^{14} cm^{-3} , while it is $8 \times 10^{19} \text{ cm}^{-3}$ after H_2 is introduced, thus becoming a high-conductivity film [37]. Figure 1 shows the relationship between the dielectric constant and the incident wavelength of IGZO before and after the introduction of H_2 . The increase in electron density leads to a decrease in the dielectric constant.

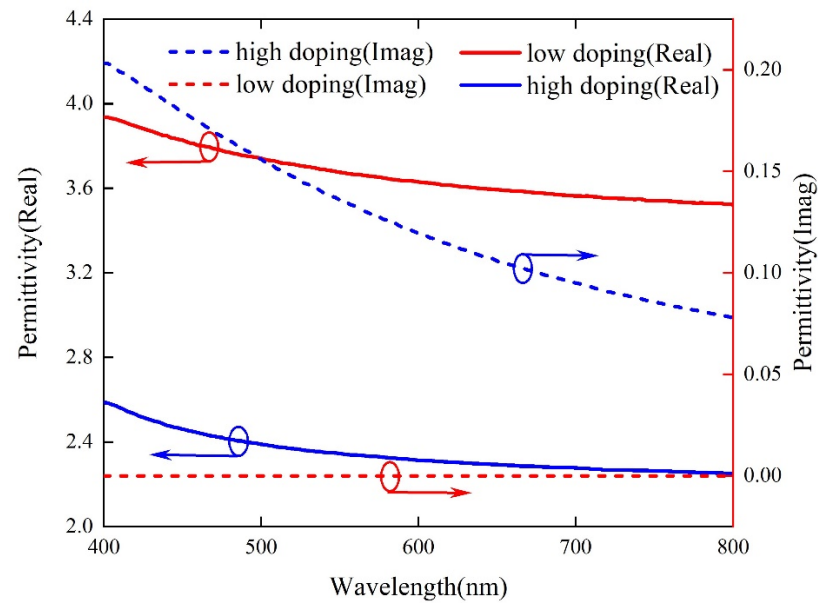


Figure 1. The real and imaginary parts of the complex dielectric constant of IGZO vary with wavelength.

The designed color-changing filter which involves inserting IGZO between the two metal layers, is shown in Figure 2a. Ag was selected as the metal reflector, as it has high reflectivity in the visible light range. Its refractive index was obtained from the literature [38]. For the scale parameters, the thickness of the top and bottom Ag was $t = 30 \text{ nm}$, the thickness of the middle IGZO was d and the substrate was SiC. In the absence of free carriers, the optical properties of SiC are given by the Drude–Lorentz model [39]:

$$\epsilon_{\text{SiC}} = \epsilon_{\infty} \frac{\omega^2 - \omega_L^2 + i\gamma\omega}{\omega^2 - \omega_T^2 + i\gamma\omega} \quad (7)$$

Here, ω_L and ω_T were selected as 972 cm^{-1} and 796 cm^{-1} , respectively; ϵ_{∞} is the high-frequency dielectric constant, selected as 3.75 cm^{-1} ; and γ is defined as the damping rate caused by vibration anharmonicity, here set to 6.5.

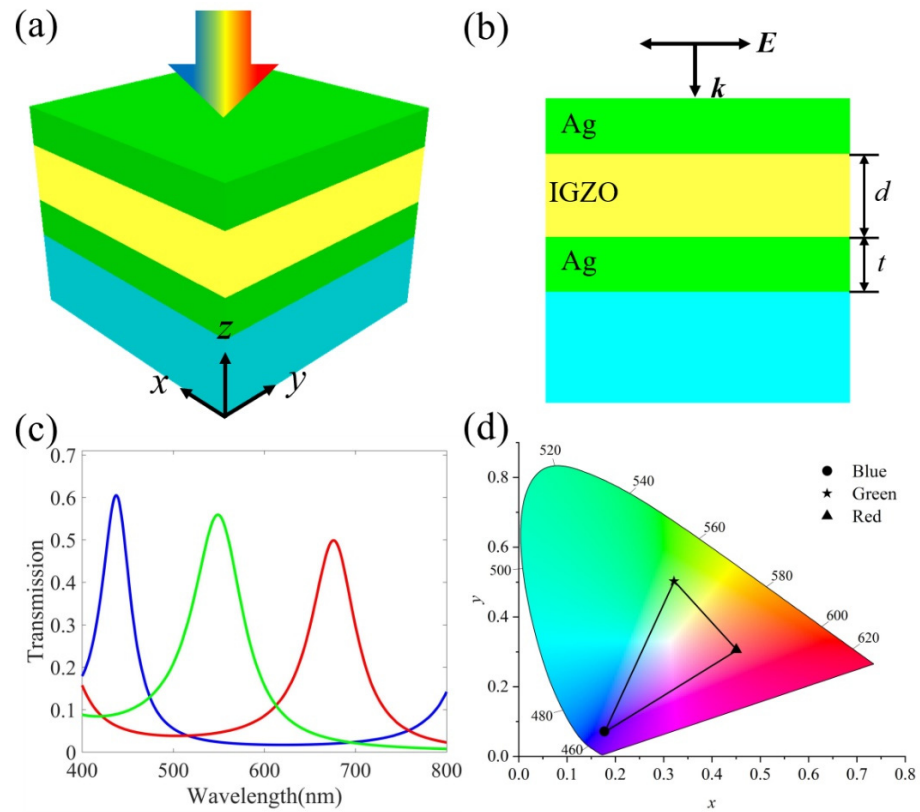


Figure 2. (a) Schematic diagram of the proposed ultra-thin, high-efficiency color-changing filter; (b) cross-sectional view of the structure; (c) the calculated transmission spectrum at normal incidence. $T = 30$ nm and $d = 170$ nm, 90 nm and 125 nm, respectively; (d) the corresponding chromaticity diagram of the RGB structural color.

Figure 3 shows the schematic of the multi-layer optical dielectric thin film with uniform dielectrics in each layer. We consider the reflection and the transmission of a TE-polarized plane wave (electric field perpendicular to the incident plane) of free space with wavelength λ_0 and incident at angle θ on L uniform layers. The thin film above the high reflective films lies in the x - z plane. For analysis, the multi-layer dielectric can be divided into L layers along the z direction. Each layer possesses a refractive index of n_1 , n_2 and n_L and a thickness of d_1 , d_2 and d_L . The normalized electric field for the input and output regions can be written as:

$$E_{I,y} = \exp[-jk_0 n_1 (\sin \theta x + \cos \theta z)] + \sum_i R_i \exp[-j(k_x x - k_{I,z} z)] \quad (Z < 0)$$

$$E_{II,y} = \sum_i T_i \exp\{-j[k_{xi} x - k_{II,zi} (z - D)]\} \quad (Z > D) \quad (8)$$

where R and T are the reflected and the transmitted amplitudes of the electric fields and $k_0 = 2\pi/\lambda_0$ is the wave-vector magnitude in the air. The wave vectors along the x and z directions in each divided layer are $k_{xi} = k_0 n_i \sin \theta$ and $k_{zi} = k_0 n_i \cos \theta$, respectively.

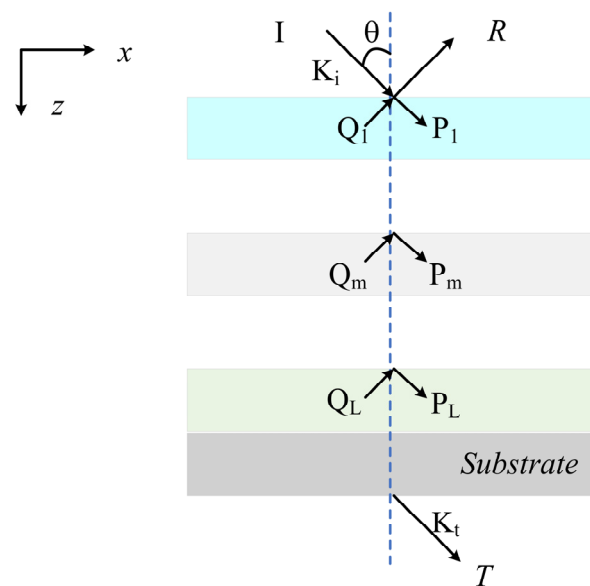


Figure 3. Geometry for the reflection and the transmission from a stack of multi-layer optical dielectric thin films.

The tangential magnetic and electric fields in the m -th ($0 < Z < D$) divided layer can be expressed in the following form:

$$\begin{aligned} E_{m,y} &= \sum_i S_{m,yi}(z) \exp(-jk_{xi}x) \\ H_{m,x} &= -j(\epsilon_0/\mu_0)^{1/2} \sum_i U_{m,xi}(z) \exp(-jk_{xi}x) \end{aligned} \quad (9)$$

Here, ϵ_0 and μ_0 are the permittivity and permeability of free space and $S_{m,yi}(z)$ and $U_{m,xi}(z)$ are the normalized amplitudes of the m -th space-harmonic fields that satisfy Maxwell's equation in each divided layer.

As in the uniform, homogenous layer, the reflected and transmitted amplitudes can be solved by matching the tangential electromagnetic fields at the boundaries between each divided layer. At the boundary between the input region and the first layer ($Z = 0$), the following equation should be satisfied:

$$\begin{bmatrix} \delta_{i0} \\ jn_1 \cos \theta \delta_{i0} \end{bmatrix} + \begin{bmatrix} I \\ -jY_1 \end{bmatrix} [R] = \begin{bmatrix} W_1 & W_1 X_1 \\ V_1 & -V_1 X_1 \end{bmatrix} \begin{bmatrix} c_1^+ \\ c_1^- \end{bmatrix} \quad (10)$$

At the boundary between the $m-1$ and the m divided layer ($Z = D_m$):

$$\begin{bmatrix} W_{m-1} X_{m-1} & W_{m-1} \\ V_{m-1} X_{m-1} & -V_{m-1} \end{bmatrix} \begin{bmatrix} c_{m-1}^+ \\ c_{m-1}^- \end{bmatrix} = \begin{bmatrix} W_m & W_m X_m \\ V_m & -V_m X_m \end{bmatrix} \begin{bmatrix} c_m^+ \\ c_m^- \end{bmatrix} \quad (11)$$

At the boundary between the last divided layer and the substrate ($Z = D_L$):

$$\begin{bmatrix} W_L X_L & W_L \\ V_L X_L & -V_L \end{bmatrix} \begin{bmatrix} c_L^+ \\ c_L^- \end{bmatrix} = \begin{bmatrix} I \\ jY_2 \end{bmatrix} [T] \quad (12)$$

where W and V are a matrix whose element is determined according to the eigenvector and eigenvalues derived from Equations (1) and (2); Y_1 and Y_2 are diagonal matrices, with the diagonal elements being $k_{L,z}/k_0$ and $k_{L,z}/k_0$, respectively, in each divided layer; and c_L is the unknown constant to be determined. Therefore, the relation can be obtained as:

$$\begin{aligned} \begin{bmatrix} f_L \\ g_L \end{bmatrix} T_L &= \begin{bmatrix} 1 & \exp(-k_0 \gamma_L d_L) \\ \gamma_L & -\gamma_L \exp(-k_0 \gamma_L d_L) \end{bmatrix} \times \begin{bmatrix} a_L \\ b_L \exp(-k_0 \gamma_L d_L) \end{bmatrix} T_L \\ &= \begin{bmatrix} a_L + b_L \exp(-k_0 \gamma_L d_L) \\ \gamma_L [a_L - b_L \exp(-k_0 \gamma_L d_L)] \end{bmatrix} T_L \end{aligned} \quad (13)$$

where $\begin{bmatrix} a_L \\ b_L \end{bmatrix} = \begin{bmatrix} 1 & 1 \\ \gamma_L & -\gamma_L \end{bmatrix}^{-1} \begin{bmatrix} f_{L+1} \\ g_{L+1} \end{bmatrix}$, and $f_{L+1} = 1, g_{L+1} = jk_{L,z}/k_0$.

We can easily obtain the relation between reflected and transmitted amplitudes from Equations (4)–(7) without any numerical instability by using the enhanced transmittance matrix approach [6], as in the following:

$$\begin{bmatrix} \delta_{i0} \\ jn_1 \cos \theta \delta_{i0} \end{bmatrix} + \begin{bmatrix} I \\ -jY_1 \end{bmatrix} [R] = \begin{bmatrix} f_1 \\ g_1 \end{bmatrix} T_1 \quad (14)$$

Here, f_1 and g_1 are the assistant parameters in the enhanced transmittance matrix approach. From Equations (6) and (7), we can obtain the reflected amplitudes R and transmittance amplitudes T . Thus, the reflectance and transmittance of the multi-layer can be solved as follows:

$$\begin{aligned} R &= RR * \text{Re}(k_{L,z}/k_0 n_L \cos \theta) \\ T &= TT * \text{Re}(k_{L,z}/k_0 n_L \cos \theta) \end{aligned} \quad (15)$$

The entire structure is deposited on SiC, and a high-purity structural color can be obtained by changing the thickness of the IGZO. Figure 2c shows the transmission spectra corresponding to different IGZO thicknesses. When $d = 170$ nm, a blue (B) structural color appears at the resonance wavelength of 438 nm, and the transmission efficiency is 60.2%. When the thickness d of IGZO is adjusted to 90 nm and 125 nm, green (G) and red (R) structural colors with 55.9% and 49.9% transmission efficiencies at 550 nm and 676 nm can be obtained, respectively. Figure 2d plots the RGB chromaticity coordinates corresponding to the transmission curves in Figure 2c. The chromaticity coordinates for blue, green and red colors are (0.177, 0.072), (0.321, 0.502) and (0.450, 0.356), respectively. A wide-color RGB gamut is produced; thus, a variety of transmission colors can be generated.

3. Results and Discussions

The color filter exhibits the shape of a common F-P resonator, which is determined by the constructive interference and the destructive interference caused by the specific phase shift at the metal interface. Figure 4a,b depict the transmission spectra when d changes in the range of 80–180 nm before and after H₂ treatment. The resonance wavelength shifts significantly with d . This wavelength is shifted after H₂ treatment. The chromaticity diagram of the corresponding transmission curve is plotted in Figure 4c, and the chromaticity coordinates are shown in black and red, respectively. To visually demonstrate the performance of the color filter resulting from the change in IGZO electron density, we converted the transmission spectrum in Figure 4a,b into color, and the result is shown in Figure 4d. When $d = 120$ nm, the resonance wavelengths before and after the H₂ treatment are 657.7 nm and 537.3 nm, respectively. The chromaticity coordinates change from (0.493, 0.326) to (0.284, 0.454), and the transmission color changes from red to green. For other values, the resonance wavelength will also shift after H₂ treatment, and the transmission color will change. Therefore, by changing the electron density of the IGZO layer, the refractive index of the film can be changed so as to achieve the transformation of structural color.

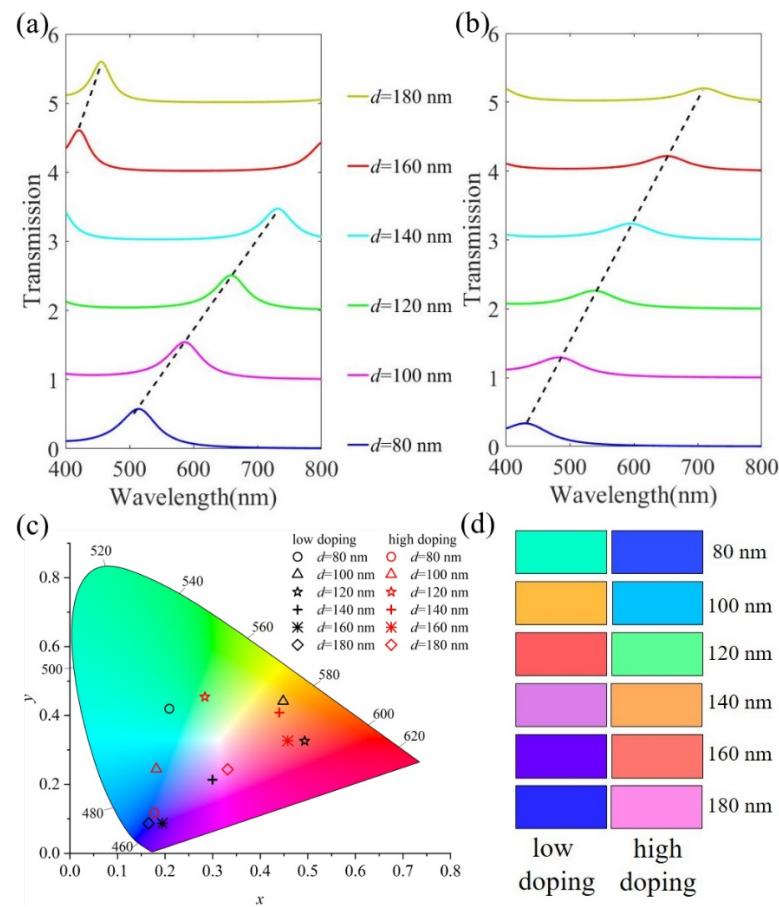


Figure 4. Simulated spectral transmittance curves at normal incidence with different d (a) before H_2 plasma treatment and (b) after H_2 plasma treatment. (c) The corresponding chromaticity diagram for RGB structural colors before and after H_2 plasma treatment. (d) The color change corresponds to the (a,b) transmission curve.

During the design, the optimal design geometries for the MSM cavity had to be obtained. To achieve this goal, the transmission spectra for different IGZO thicknesses before and after H_2 treatment at normal incidence were determined. The structures were excited with a plane wave in the frequency range of interest, which was 400–800 nm. As shown in Figure 5a,b, the resonant peak was obtained by gradually increasing the thickness of IGZO under TM polarization in the visible range considered. The shift in the resonance wavelength before and after H_2 treatment showed a tendency to shrink, and the transmission effect was weakened. High-purity RGB colors were obtained, as shown in Figure 5a, and the resonance peak could be shifted by adjusting the thickness. Therefore, the resonance wavelength shifts significantly after H_2 treatment. For TE-polarized light, the same result was obtained under TM polarization, as shown in Figure 5c,d. The polarization of the implemented filter was independent.

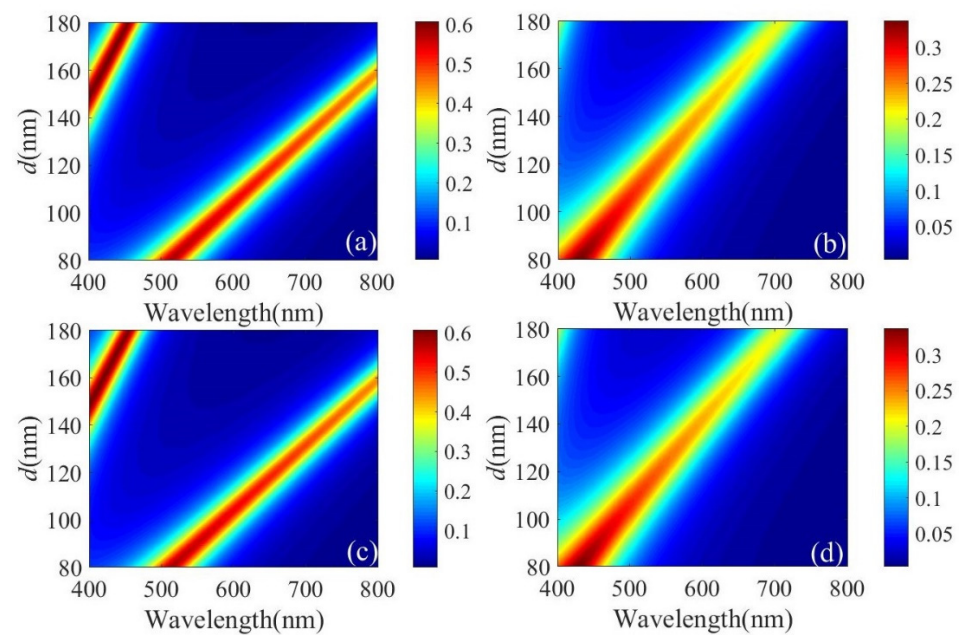


Figure 5. For TM polarization: (a) transmission spectra of different IGZO thicknesses before H₂ treatment and (b) after H₂ treatment. For TE-polarization: (c) transmission spectra of different IGZO thicknesses before H₂ treatment and (d) after H₂ treatment.

The thickness of the metal layer reflector affects the transmission effect and the color produced. In the following, we study the effect of the metal layer thickness t on the transmission spectrum and color-rendering properties. Figure 6a depicts the change in the transmittance of RGB with the thickness of Ag at normal incidence when the filter presents the G color. As t increases, the transmission efficiency decreases and the resonance wavelength is red-shifted. Figure 6b shows the transmission spectrum after H₂ treatment; with the increase in t , the transmission efficiency also decreases, but the spectral response additionally becomes clearer, resulting in improved color purity. As shown in Figure 6c, this is the color coordinate described in the CIE 1931 chromaticity diagram. When $t = 20$ nm, although the transmission efficiency is very high, it deviates from the original green. The H₂ treatment also has the same result. The variation in the resonance results in a deviation from the original blue color. Therefore, we must fully consider the influence of the thickness of the reflector on the color-rendering effect.

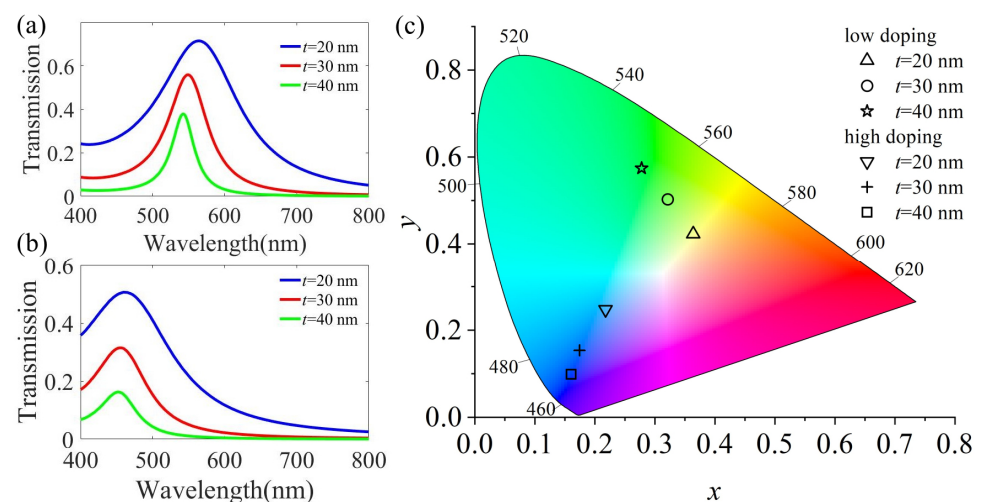


Figure 6. (a) Simulated spectral transmittance curves at normal incidence with different t for green, $d = 90$ nm. (b) The corresponding transmission spectrum after plasma treatment with H₂. (c) An illustration of color coordinates calculated from the transmission spectra studied in (a,b).

In order to study the physical properties of the adjustable structure before and after H₂ treatment, the electric field distribution diagram at the resonance wavelength of 550 nm (G color) was studied. Figure 7a,b show the electric field changes before and after H₂ treatment. It can be seen that the highest electric field intensity in the low-conductivity film reaches 2.7, which is significantly stronger than that of the high-conductivity film. The electric field in Figure 7a is mainly concentrated at the junction of the metal cavity and IGZO and FP resonance occurs, enhancing transmission efficiency, while the light field in Figure 7b is mainly located in the top Ag cavity, which leads to weakened resonance and a weakened transmission effect.

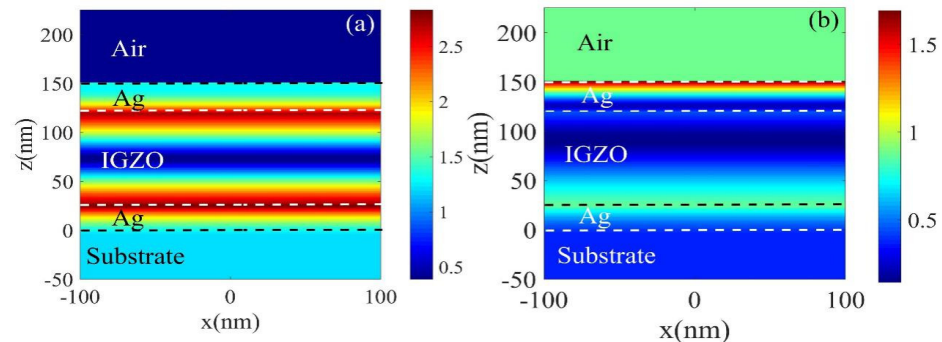


Figure 7. The electric field distribution curve for the color filter (green) with a resonance wavelength of 550 nm in the x - z plane, $t = 30$ nm, $d = 90$ nm: (a) before H₂ treatment; (b) after H₂ treatment.

Next, we studied the relationship between the transmission spectra before and after the H₂ treatment and the incident angle. From Figure 8a,c,e, it can be seen that, for low-conductivity films, within the incident angle range of 0–60°, the resonance wavelength remains almost unchanged, and the transmission efficiency does not change much. High-purity RGB structural colors can be obtained and good resonance characteristics maintained. When the B color appears, as the incident angle increases, resonance appears at 780–800 nm, but the color filter effect is not affected. Figure 8b,d,f correspond to the transmission spectra of IGZO treated with H₂ shown in Figure 8a,c,e, respectively. The position of the resonance peak shows a significant color shift. When the incident angle changes from 0 to 60°, the resonant peak position of RGB color is almost unchanged. It is thus proved that the structure has good incident angle insensitivity.

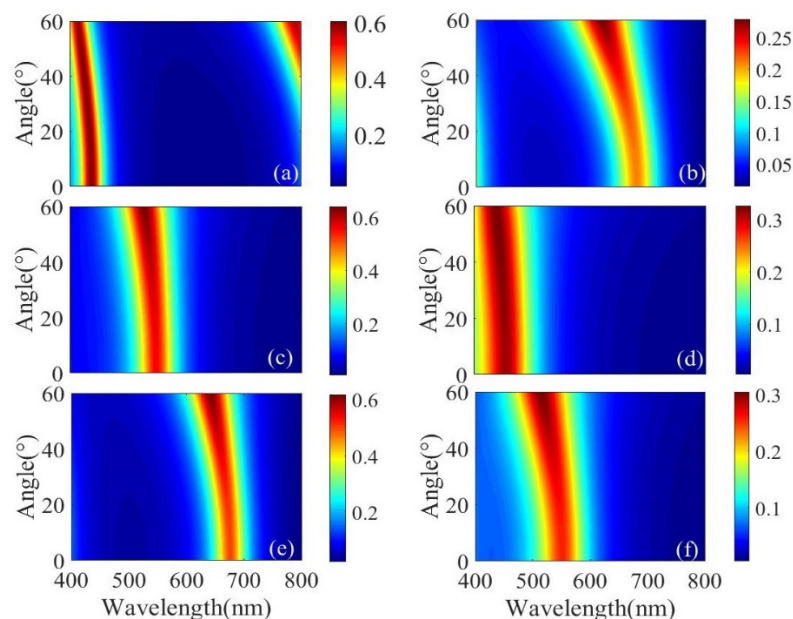


Figure 8. For low-conductivity films, the transmission spectra are functions of the wavelength and incident angle of (a) B, (c) G and (e) R colors, respectively. For high-conductivity films, the transmission spectra are functions of the wavelength and incident angle of (b) R, (d) B and (f) G colors, respectively.

4. Conclusions

In summary, numerical research was carried out on ultra-thin and efficient color-changing filters. The Ag-IGZO-Ag resonator covering the IGZO layer was used to achieve FP resonance. An adjustable bandwidth in the fixed-resonance wavelength could be realized, and any color in the visible light band could be obtained. The output color had the advantages of rich color, wide color gamut, high color saturation and high purity. Through the H₂ treatment, the IGZO could become a high-conductivity film, so that the color could be switched, the resonance wavelength shifted and a transmission palette obtained. Moreover, it was determined from the RCWA that, when the incident angle was changed between 0 and 60°, the wavelength of the resonant peak remained basically unchanged; thus, it has good incident angle-insensitive characteristics. The proposed structure has significant application prospects and great potential for displays, image sensors and decorations.

Author Contributions: Conceptualization, X.F., G.Z. and S.W.; software, D.X., X.F., and G.Z.; formal analysis, X.F. and G.Z.; investigation, X.F., S.W. and G.Z.; methodology, D.X. and G.Z.; resources, G.Z.; writing—original draft preparation, X.F. and S.W.; writing—review and editing, D.X. and G.Z.; visualization, X.F. and S.W.; supervision, G.Z.; project administration, G.Z. All authors have read and agreed to the published version of the manuscript.

Funding: This research received no external funding.

Data Availability Statement: The data that support the findings of this study are available from the corresponding author upon reasonable request.

Acknowledgments: The authors thank YOUQ MA for useful discussions.

Conflicts of Interest: The authors declare no conflicts of interest.

References

1. Tan, S.J.; Zhang, L.; Zhu, D.; Goh, X.M.; Wang, Y.M.; Kumar, K.; Qiu, C.W.; Yang, J.K.W. Plasmonic color palettes for photorealistic printing with aluminum nanostructures. *Nano Lett.* **2014**, *14*, 4023–4029.
2. James, T.D.; Mulvaney, P.; Roberts, A. The plasmonic pixel: Large area, wide gamut color reproduction using aluminum nanostructures. *Nano Lett.* **2016**, *16*, 3817–3823.
3. Flauraud, V.; Reyes, M.; Paniagua-Domínguez, R.; Kuznetsov, A.I.; Brugger, J. Silicon nanostructures for bright field full color prints. *ACS Photonics* **2017**, *4*, 1913–1919.
4. Duan, X.; Kamin, S.; Liu, N. Dynamic plasmonic colour display. *Nat. Commun.* **2017**, *8*, 14606.
5. Franklin, D.; Frank, R.; Wu, S.T.; Chanda, D. Actively addressed single pixel full-colour plasmonic display. *Nat. Commun.* **2017**, *8*, 15209.
6. Kristensen, A.; Yang, J.K.W.; Bozhevolnyi, S.I.; Link, S.; Nordlander, P.; Halas, N.J.; Asger Mortensen, N. Plasmonic colour generation. *Nat. Rev. Mater.* **2016**, *2*, 16088.
7. Montelongo, Y.; Yetisen, A.K.; Butt, H.; Yun, S.H. Reconfigurable optical assembly of nanostructures. *Nat. Commun.* **2016**, *7*, 12002.
8. Wang, Y.M.; Tian, X.T.; Zhang, H.; Yang, Z.R.; Yin, X.B. Anticounterfeiting quick response code with emission color of invisible metal-organic frameworks as encoding information. *ACS Appl. Mater. Interfaces* **2018**, *10*, 22445–22452.
9. Xu, T.; Wu, Y.K.; Luo, X.; Guo, L.J. Plasmonic nanoresonators for high-resolution colour filtering and spectral imaging. *Nat. Commun.* **2010**, *1*, 59.
10. Heydari, E.; Sperling, J.R.; Neale, S.L.; Clark, A.W. Plasmonic color filters as dual-state nanopixels for high-density microimage encoding. *Adv. Funct. Mater.* **2017**, *27*, 1701866.
11. Lee, K.T.; Han, S.Y.; Park, H.J. Omnidirectional flexible transmissive structural colors with high-color-purity and high-efficiency exploiting multicavity resonances. *Adv. Opt. Mater.* **2017**, *5*, 1700284.
12. Wan, W.Q.; Luo, M.H.; Liu, Z.M.; Su, Y.F. Ultrathin high-efficiency, variable-color filters with an adjustable bandwidth by combining a cavity resonator and a dielectric film. *Opt. Commun.* **2020**, *459*, 124884.
13. Tseng, M.L.; Yang, J.; Semmlinger, M.; Zhang, C.; Nordlander, P.; Halas, N.J. Two-dimensional active tuning of an aluminum plasmonic array for full-spectrum response. *Nano Lett.* **2017**, *17*, 6034.

14. Roberts, A.S.; Pors, A.; Albrektsen, O.; Bozhevolnyi, S.I. Subwavelength plasmonic color printing protected for ambient use. *Nano Lett.* **2014**, *14*, 783–787.
15. Wang, C.T.; Hou, H.H.; Chang, P.C.; Li, C.C.; Jau, H.C.; Hung, Y.J.; Lin, T.H. Full-color reflectance-tunable filter based on liquid crystal cladded guided-mode resonant grating. *Opt. Express* **2016**, *24*, 22892.
16. Uddin, M.J.; Khaleque, T.; Magnusson, R. Guided-mode resonant polarization- controlled tunable color filters. *Opt. Express* **2014**, *22*, 12307–12315.
17. Park, C.S.; Koirala, I.; Gao, S.; Shrestha, V.R.; Lee, S.S.; Choi, D.Y. Structural color filters based on an all-dielectric metasurface exploiting silicon-rich silicon nitride nanodisks. *Opt. Express* **2019**, *27*, 667–679.
18. Sun, S.; Yang, W.H.; Zhang, C.; Jing, J.X.; Gao, Y.S.; Yu, X.Y.; Song, Q.H.; Xiao, S.M. Real-time tunable colors from microfluidic reconfigurable all-dielectric metasurfaces. *ACS Nano* **2018**, *12*, 2151.
19. Dong, Z.G.; Ho, J.F.; Yu, Y.F.; Fu, Y.H.; Paniagua-Dominguez, R.; Wang, S.H.; Kuznetsov, A.I.; Yang, J.K.W. Printing beyond sRGB color gamut by mimicking Silicon nanostructures in free-space. *Nano Lett.* **2017**, *17*, 7620.
20. Chen, M.; Wen, L.; Pan, D.; Cumming, David R. S.; Yang, X.; Chen, Q. Full-color nanorouter for high-resolution imaging. *Nanoscale*, **2021**, *13*, 13024–13029.
21. Chen, Y.Q.; Duan, X.Y.; Matuschek, M.; Zhou, Y.M.; Neubrech, F.; Duan, H.G.; Liu, N. Dynamic color displays using stepwise cavity resonators. *Nano Lett.* **2017**, *17*, 5555.
22. Jung, Y.; Jung, H.; Choi, H.; Lee, H. Polarization selective color filter based on plasmonic nanograting embedded etalon structures. *Nano Lett.* **2020**, *20*, 6344–6350.
23. Lee, H.E.; Ahn, H.Y.; Mun, J.; Lee, Y.Y.; Kim, M.; Cho, N.H.; Chang, K.; Kim, W.S.; Rho, J.; Nam, K.T. Amino-acid- and peptide-directed synthesis of chiral plasmonic gold nanoparticles. *Nature* **2018**, *556*, 360–365.
24. Kim, M.; Kim, I.; Jang, J.; Lee, D.; Nam, K.T.; Rho, J. Active color control in a metasurface by polarization rotation. *Appl. Sci.* **2018**, *8*, 982.
25. Jang, J.; Jeong, H.; Hu, G.; Qiu, C.W.; Nam, K.T.; Rho, J. Tunable metasurfaces: Kerker-conditioned dynamics cryptographic nanoprints. *Adv. Opt. Mater.* **2019**, *7*, 1970016.
26. Raeis-Hosseini, N.; Lim, S.; Hwang, H.; Rho, J. Reliable Ge₂Sb₂Te₅-integrated high-density nanoscale conductive bridge random access memory using facile nitrogen-doping strategy. *Adv. Electron. Mater.* **2018**, *4*, 1800360.
27. Hosseini, P.; Wright, C.D.; Bhaskaran, H. An optoelectronic framework enabled by low-dimensional phase-change films. *Nature* **2014**, *511*, 206–211.
28. Hopmann, E.; Elezzabi, A.Y. Plasmochromic nanocavity dynamic light color switching. *Nano Lett.* **2020**, *20*, 1876–1882.
29. Yoon, G.; So, S.; Kim, M.; Mun, J.; Ma, R.M.; Rho, J. Electrically tunable metasurface perfect absorber for infrared frequencies. *Nano Converg.* **2017**, *4*, 36.
30. Yu, Y.L.; Yu, Y.F.; Huang, L.J.; Peng, H.W.; Xiong, L.W.; Cao, L.Y. Giant gating tunability of optical refractive index in transition metal dichalcogenide monolayers. *Nano Lett.* **2017**, *17*, 3613–3618.
31. Zhu, Y.; He, Y.L.; Jiang, S.S.; Zhu, L.; Chen, C.S.; Wan, Q. Indium-gallium-zinc-oxide thin-film transistors: Materials, devices, and applications. *J. Semicond.* **2021**, *42*, 031101.
32. Huang, C.Y.; Peng, T.Y.; Hsieh, W.T. Realization of a self-powered InGaZnO MSM UV photodetector using localized surface fluorine plasma treatment. *ACS Appl. Electron. Mater.* **2020**, *2*, 2976–2983.
33. Peng, T.Y.; Huang, C.Y. Increasing the gas response of ozone sensors based on solution-processed InGaZnO by tuning the size of the nanostructure. *ECS J. Solid State Sci. Technol.* **2022**, *11*, 067001.
34. Kamiya, T.; Nomura, K.; Hosono, H. Present status of amorphous In-Ga-Zn-O thin-film transistors. *Sci. Technol. Adv. Mater.* **2010**, *11*, 044305.
35. Fujiwara, H.; Kondo, M. Effects of carrier concentration on the dielectric function of ZnO: Ga and In₂O₃: Sn studied by spectroscopic ellipsometry: Analysis of free-carrier and band-edge absorption. *Phys. Rev. B* **2005**, *71*, 075109.
36. Li, X.D.; Chen, S.; Chen, T.P.; Liu, Y. Thickness dependence of optical properties of amorphous indium gallium zinc oxide thin films: Effects of free-electrons and quantum confinement. *ECS Solid State Lett.* **2015**, *4*, 29–32.
37. Kim, I.; Yun, J.; Badloe, T.; Park, H.; Seo, T.; Yang, Y.; Kim, J.; Chung, Y.; Rho, J. Structural color switching with a doped indium-gallium-zinc-oxide semiconductor. *Photon. Res.* **2020**, *8*, 1409–1415.
38. Lee, K.T.; Han, S.Y.; Li, Z.J.; Baac, H.W.; Park, H.J. Flexible high-color-purity structural color filters based on a higher-order optical resonance suppression. *Sci. Rep.* **2019**, *9*, 14917.
39. Neuner, B.; Korobkin, D.; Fietz, C.; Carole, D.; Ferro, G.; Shvets, G. Critically coupled surface phonon-polariton excitation in silicon carbide. *Opt. Lett.* **2009**, *34*, 2667–2669.